Physics of Fluids

Instability of a meandering channel with variable width and curvature: Role of sediment suspension

Cite as: Phys. Fluids **33**, 111401 (2021); https://doi.org/10.1063/5.0074974
Submitted: 12 October 2021 • Accepted: 31 October 2021 • Published Online: 17 November 2021

Rajesh K. Mahato, Subhasish Dey and Sk Zeeshan Ali

Physics of Fluids PERSPECTIVE scitation.org/journal/phf

Instability of a meandering channel with variable width and curvature: Role of sediment suspension

Cite as: Phys. Fluids 33, 111401 (2021); doi: 10.1063/5.0074974
Submitted: 12 October 2021 · Accepted: 31 October 2021 ·
Published Online: 17 November 2021

Rajesh K. Mahato,[1,a] Subhasish Dey,[1,b] and Sk Zeeshan Ali[2,c]

AFFILIATIONS

[1]Department of Civil Engineering, Indian Institute of Technology Kharagpur, West Bengal 721302, India
[2]Department of Civil Engineering, Indian Institute of Technology Hyderabad, Telangana 502284, India

[a]rkm22@iitkgp.ac.in
[b]Author to whom correspondence should be addressed: sdey@iitkgp.ac.in
[c]zeeshan@ce.iith.ac.in

ABSTRACT

In this Perspective, we explore the instability of a meandering channel with variable width and curvature. The analysis employs the depth-averaged formulations for the flow and sediment transport. Unlike the conventional instability analysis that considers mainly the bedload transport, we consider the generic sediment transport including both the bedload and suspended load. The analysis addresses the variations of the near-bank excess azimuthal velocity and the bed topography deviation with the meander wavenumber for different pertinent parameters, such as Shields number, relative roughness number, channel aspect ratio, width-variation amplitude, and shear Reynolds number. The analysis detects a resonance phenomenon for certain critical values of the pertinent parameters and explores the sensitivity of the resonant wavenumber to the pertinent parameters. In a hydraulically smooth flow regime, the sediment suspension is found to play a stabilizing role. On the contrary, in hydraulically transitional and rough flow regimes, the sediment suspension offers a destabilizing effect. The stability diagrams reveal that the stable zone enlarges as the Shields number and relative roughness number increase, while it contracts with an increase in width-variation amplitude. For a given shear Reynolds number in a hydraulically smooth flow regime, the stability diagram predicts various stable zones. By contrast, for a given shear Reynolds number in hydraulically transitional and rough flow regimes, a unique stable zone exists.

I. INTRODUCTION

Natural streams are often classified into three distinct categories: straight, meandering, and braided streams. Among them, a meandering stream has attracted researchers for decades (Fig. 1). In general, a meandering channel is recognized as a channel with a sinuosity more than 1.5. The sinuosity quantifies the ratio of the curved distance to the linear distance between the end points of a curve forming the wavelength. The dynamics of a meandering channel is linked with the flow and the sediment transport.[1] The flow in a meandering channel is featured by a helicoidal motion with a superelevated free surface. The streamlines close to the free surface and the channel bed are directed toward the outer and inner banks, respectively. Hence, the outer bank is eroded continuously, and the eroded sediment is deposited at the inner bank. The continuous erosion and deposition at opposite channel banks trigger the migration of a meandering channel. A plethora of studies in the past explored the dynamics of curved channel flows.[2–12] In addition, comprehensive reviews on the topic are available in literature.[13–15]

The development of meandering was explored from two different theories: bar instability theory[16–19] and bend instability theory.[2–9] The former proposed that the formation of alternate bars in a straight channel with non-erodible banks leads to the development of meanders. Ikeda *et al.*[2] identified that the bar theory is inadequate as they do not allow the channel banks to deform. By relaxing the constraint of non-erodible banks, they presented the bend instability theory to investigate the stability of a small amplitude meandering channel with respect to a straight channel. Parker *et al.*[3] extended the mathematical development of Ikeda *et al.*[2] to obtain a nonlinear equation of bend migration. They found that the lateral and downstream migration rates amplify with the development of bend amplitude. Blondeaux and Seminara[4,5] reported a resonance phenomenon for critical magnitudes of the relevant parameters. They reported that the growth of a bend is linked with the resonance phenomenon. For channels with a small sinuosity, they noticed that the bar and bend instabilities occur at similar wavelengths. For a small channel curvature, Seminara and Tubino[8] presented a weakly-nonlinear theory of bend instability in the

FIG. 1. Photograph of a meandering stream. Courtesy: Vladimir Nikora, University of Aberdeen, UK.

neighborhood of the resonant condition. They concluded that the nonlinearities diminish the peak of the azimuthal velocity and bed topography perturbations. Zolezzi and Seminara[9] classified the channels with aspect ratios (i.e., ratio of channel half-width to flow depth) smaller and larger than the resonant aspect ratio as the sub-resonant and super-resonant channels, respectively. Moreover, they reported that the small amplitude bed waves propagate downstream and upstream for sub-resonant and super-resonant channels, respectively. Seminara *et al.*[20] employed the mathematical formulation of Zolezzi and Seminara[9] to investigate the planimetric evolution of meandering channels. They found that the meanders migrate downstream and upstream for sub-resonant and super-resonant channels, respectively. In addition, they found that the upstream and downstream skewing are associated with the sub-resonant and super-resonant channels, respectively. Bolla Pittaluga *et al.*[21] proposed a nonlinear bend instability theory. They reported that the growth of meandering channels diminishes with the amplification of their amplitude. Moreover, in accordance with the linear instability results, they found that the channels may migrate downstream or upstream depending on the magnitude of the channel aspect ratio. Dey and Ali[22] presented a phenomenological theory regarding the onset of meandering of a straight channel. They reported that the onset of meandering is linked with the counter-rotational motions of turbulent eddies that trigger alternate erosion and deposition of the channel banks. In another attempt, Ali and Dey[23] explored the effects of flow regime on the hydrodynamic instability of a meandering channel. They studied the azimuthal velocity perturbation, bed topography perturbation, bend amplification rate, and meander propagation speed in different flow regimes. In addition, they found the existence of resonance in different flow regimes.

Several studies have explored the effects of spatial width variation on the bend instability.[24–28] In a straight channel, Repetto *et al.*[24] investigated the role of spatial width variation toward the development of channel bifurcations. They observed that the widest and narrowest sections are subjected to deposition and erosion, respectively. Luchi *et al.*[25] reported the effects of spatial width variation on the dynamics of meandering channels. Based on the field observations, they reported that the frequency of the width variation is twofold that of the curvature. Moreover, they argued that the variations of the amplitudes of width and curvature are small parameters, and suggested the expansion of the pertinent variables in terms of the variations of the amplitudes of width and curvature. Furthermore, their theoretical analysis revealed that the spatial width variation triggers the instability of shorter bends with respect to constant width meanders. The role of spatial width variation was further explored by Frascati and Lanzoni.[26] Frascati and Lanzoni[26] compared the analytical model with the bed topography in a long reach of the Po River. They found that the analytical model properly describes the topography in wide, weakly curved, and long river bends with weak width variation. Moreover, Eke *et al.*[27] investigated the coevolution of channel width and planform in a meandering channel. They coupled the evolution of the channel width to the channel migration by means of a separate submodel for the bank erosion and deposition. Their analysis revealed that the ratio of the rate of migration of the eroding bank to that of the depositing bank controls the mode of spatial width variation. Considering the variable width, Monegaglia *et al.*[28] presented a novel planform evolution model. They observed that the pattern of planform evolution of a meandering channel is dependent on the channel aspect ratio. Moreover, they represented the coevolution of the autogenic width variation and curvature by means of a temporal hysteresis cycle. They found that the peak of the width variation occurs earlier than that of the channel curvature.

From the literature survey, it is evident that significant efforts have been made to explore the instability of meandering channels and their planform evolution. The theoretical studies mainly considered bedload as the only mode of sediment transport. The field study of Constantine *et al.*[29] reported that the annual migration rate of channels amplifies with an increase in the sediment load. The role of sediment suspension toward the instability of meandering channels remains unexplored theoretically. Hence, the effects of the variations in channel width and curvature on the bend instability in the presence of sediment suspension are yet to be explored.

The present study aims at exploring the instability of a meandering channel with variable width and curvature by considering the subtle role of sediment suspension. The stability analysis is performed considering a turbulent flow in a meandering channel with variable width and curvature. The depth-averaged formulations for the flow and sediment transport are employed. The analysis addresses the effects of several key parameters, such as Shields number, relative roughness number, channel aspect ratio, width-variation amplitude, and shear Reynolds number, on the bend instability. In addition, the study discloses the role of sediment suspension in different flow regimes, namely, the hydraulically smooth, transitional, and rough flow regimes.

This paper is arranged as follows: The mathematical formulation is given in Sec. II. The perturbation solution is explained in Sec. III. The results and discussion are presented in Sec. IV. Finally, conclusions are drawn in Sec. V.

II. MATHEMATICAL FORMULATION

We consider an incompressible turbulent flow through an erodible meandering channel with a variable width $2B^*$. Hereafter, a superscript asterisk indicates a dimensional quantity. The channel is composed of cohesionless uniform sediment of size d^*. We employ an intrinsic orthogonal curvilinear system of coordinates (s^*, n^*, z^*), where s^* denotes the azimuthal distance along the channel centerline, n^* represents the coordinate orthogonal to s^*, and z^* measures the vertical distance from a fixed reference level (Fig. 2). The origin of the coordinate system lies on the channel centerline [see the dashed–dotted line in Fig. 2(a)]. In Fig. 2(a), B_0^* and $B_{\max}^*$ represent the reach-averaged and maximum channel half-width, respectively, and the channel banks are marked by solid lines. In addition, the dashed lines indicate the channel banks for a constant width meander. Figure 2(b) depicts an illustrative cross-section A_1–A_2 of the meandering channel. The flow in a meandering channel is characterized by a spiral motion owing to the effects of radial acceleration. The flow streamlines close to the free surface are deflected toward the outer bank, while those close to channel bed is directed toward the inner bank. Therefore, the outer and inner banks are subjected to continuous erosion and deposition, respectively [Fig. 2(b)]. Moreover, the radial acceleration results in a superelevation of the free surface toward the outer bank, as sketched in Fig. 2(b). The local flow depth and the free surface elevation from the reference level are denoted by D^* and H^*, respectively, and the undisturbed channel cross-section is shown by the dashed line. The reach-averaged flow depth and velocity are considered to be D_0^* and U_0^*, respectively.

The notations assigned for the components of depth-averaged flow velocity, bed shear stress, bedload flux, and suspended load flux in (s^*, n^*) directions are (U_s^*, U_n^*), (T_s^*, T_n^*), (Q_{bs}^*, Q_{bn}^*), and (Q_{ss}^*, Q_{sn}^*), respectively. The dynamics of a meandering channel is studied using the shallow water approximation, as the spatial scale of meandering is of the order of several channel widths. The meander planform evolves on a much larger time scale with respect to the time scales related to the flow and bed deformation. Hence, the quasi-steady assumption for the flow can be employed. In large-scale morphodynamic models, the literature supports the use of the depth-averaged continuity and momentum equations. To proceed further, we define the following dimensionless quantities:

$$\begin{gathered} s=\frac{s^*}{B_0^*},\quad n=\frac{n^*}{B^*},\quad D=\frac{D^*}{D_0^*},\quad H=\frac{H^*}{F^2D_0^*},\\ F=\frac{U_0^*}{(g^*D_0^*)^{0.5}},\quad \beta=\frac{B_0^*}{D_0^*},\quad B=\frac{B^*}{B_0^*},\quad (U_s,U_n)=\frac{(U_s^*,U_n^*)}{U_0^*},\\ (T_s,T_n)=\frac{(T_s^*,T_n^*)}{\rho_f U_0^{*2}},\quad (\Phi_{bs},\Phi_{bn})=\frac{(Q_{bs}^*,Q_{bn}^*)}{(\Delta g^* d^{*3})^{0.5}},\\ (\Phi_{ss},\Phi_{sn})=\frac{(Q_{ss}^*,Q_{sn}^*)}{U_0^*D_0^*},\quad \text{and}\quad \gamma=\frac{(\Delta g^* d^{*3})^{0.5}}{(1-p)U_0^*D_0^*}, \end{gathered} \tag{1}$$

where F is the unperturbed flow Froude number, g^* is the acceleration due to gravity, β is the channel aspect ratio, ρ_f is the mass density of fluid, Δ is the submerged relative density [$= (\rho_p/\rho_f) - 1$], ρ_p is the mass density of sediment particles, p is the sediment porosity, and γ is the ratio of the scale of the sediment flux to that of the flow flux. Furthermore, two crucial parameters are introduced, namely, the curvature ratio ν and the amplitude of channel width variation δ. They are defined as

$$\nu=\frac{B_0^*}{R_0^*}\quad\text{and}\quad \delta=\frac{B_{\max}^*-B_0^*}{2B_0^*}, \tag{2}$$

where R_0^* is twofold the radius of curvature at the bend apex of the channel centerline. Then, the dimensionless channel half-width and curvature are defined as

$$B(s)=1+\delta b(s)\quad\text{and}\quad C(s)=C^*(s^*)R_0^*, \tag{3}$$

where $\delta b(s)$ denotes the dimensionless deviation from the reach-averaged channel half-width.

The depth-averaged momentum equations of the fluid phase in s- and n-direction read[25,26,28]

$$U_s\frac{\partial U_s}{\partial s}+U_n\frac{\partial U_s}{\partial n}+\frac{\partial H}{\partial s}+\beta\frac{T_s}{D}=\nu g_{10}+\delta g_{01}+\nu\delta g_{11}+\nu^2 g_{20}, \tag{4}$$

$$U_s\frac{\partial U_n}{\partial s}+U_n\frac{\partial U_n}{\partial n}+\frac{\partial H}{\partial n}+\beta\frac{T_n}{D}=\nu h_{10}+\delta h_{01}+\nu\delta h_{11}+\nu^2 h_{20}, \tag{5}$$

respectively, where the terms g_{10}, g_{01}, g_{11}, g_{20}, h_{10}, h_{01}, h_{11}, and h_{20} quantify the forcing effects owing to the curvature and width variations. Their algebraic expressions are given in Appendix A.

The depth-averaged continuity equation of the fluid phase is expressed as[25,26,28]

$$\frac{\partial}{\partial s}(DU_s)+\frac{\partial}{\partial n}(DU_n)=-\nu\left[CDU_n+nC\frac{\partial}{\partial n}(DU_n)\right]+\delta\left[n\frac{db}{ds}\cdot\frac{\partial}{\partial n}(DU_s)+b\frac{\partial}{\partial n}(DU_n)\right]. \tag{6}$$

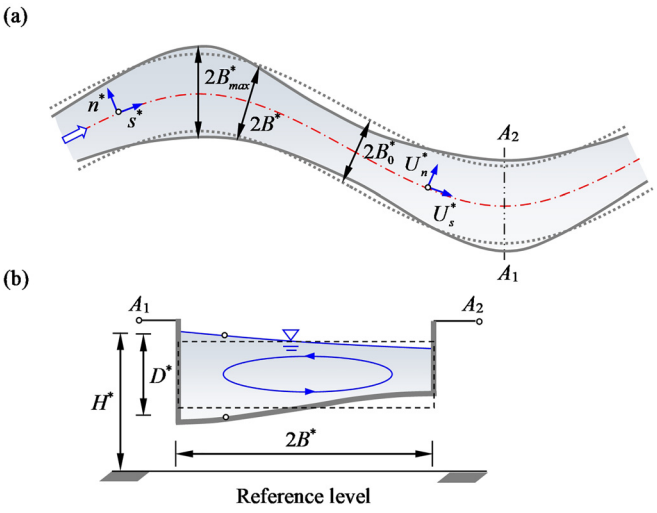

FIG. 2. Definition sketch of the physical system: (a) plan view and (b) cross-sectional view.

To study the stability and dynamics of meandering channels, the momentum and continuity equations of the fluid phase are required to be coupled with the continuity equation of the solid phase. The depth-averaged continuity equation of the solid phase reads[25,26,28]

$$\frac{\partial \Phi_s}{\partial s}+\frac{\partial \Phi_n}{\partial n}=-\nu\left(C\Phi_n+nC\frac{\partial \Phi_n}{\partial n}\right)+\delta\left(n\frac{\mathrm{d}b}{\mathrm{d}s}\cdot\frac{\partial \Phi_s}{\partial n}+b\frac{\partial \Phi_n}{\partial n}\right), \quad (7)$$

where $\Phi_s=\gamma\Phi_{bs}+\Phi_{ss}/(1-p)$ and $\Phi_n=\gamma\Phi_{bn}+\Phi_{sn}/(1-p)$.

To close the above system of equations, suitable closure relations for the bed shear stress and sediment flux vectors are essential. We express the bed shear stress vector as[32]

$$(T_s, T_n)=C_f(U_s^2+U_n^2)^{0.5}(U_s, U_n+\tau), \quad (8)$$

where C_f is the friction coefficient and τ is the contribution of the secondary flow to the radial bed shear stress. The τ is expressed as[9]

$$\tau=\nu\left[\frac{CDU_s}{\beta C_f^{0.5}}\left(k_3+\frac{k_5}{\beta C_f^{0.5}}\cdot\frac{\partial D}{\partial s}\right)+\frac{k_4D^2}{\beta^2C_f}\cdot\frac{\partial}{\partial s}(CU_s)\right], \quad (9)$$

where k_3, k_4, and k_5 are the coefficients. To estimate the friction coefficient C_f, we employ the Colebrook–White equation.[30] This reads

$$\frac{1}{(8C_f)^{0.5}}=-0.86\ln\left[\left(\frac{k_s}{14.8D}\right)^{1.1}+\frac{1}{(8C_f)^{0.5}}\cdot\frac{2.51}{R}\right], \quad (10)$$

where $k_s=k_s^*/D_0^*$, k_s^* is the bed roughness height, R is the flow Reynolds number ($=4\,U_s^*D^*/\upsilon$), and υ is the coefficient of kinematic viscosity of fluid. We express the bed roughness height k_s^* in terms of the particle size d^* as $k_s^*=\alpha d^*$, where α is an empirical coefficient equaling 2.5.[31] In this context, it is important to mention that the use of Colebrook–White equation helps to estimate the friction coefficient over a broad range of flow regimes. The flow regimes are classified as hydraulically smooth ($R_*\leq 5$), transitional ($5<R_*<70$), and rough flow regimes ($R_*\geq 70$), where R_* is the shear Reynolds number. The R_* is defined as[32]

$$R_*=\frac{u_f^*k_s^*}{\upsilon}, \quad (11)$$

where u_f^* is the shear velocity.

The flow over an erodible channel-bed exerts hydrodynamic force on the sediment particles. The Shields number Θ quantifies the dimensionless fluid-induced bed shear stress. It is defined as[32]

$$\Theta=\frac{u_f^{*2}}{\Delta g^*d^*}. \quad (12)$$

Note that the shear Reynolds number R_* and the Shields number Θ can be readily coupled as $R_*=\alpha(\Theta D_*^3)^{0.5}$, where D_* is the particle parameter [$=d^*(\Delta g^*/\upsilon^2)^{1/3}$]. Based on the properties of sediment particles and flow conditions, the particles are transported as bedload and suspended load. Herein, we consider both the modes of sediment transport. The particles are entrained into the flow when the Shields number surpasses the threshold Shields number Θ_c. The determination of Θ_c requires an analysis of the complex force system acting on the particles.[33–36] In this formulation, we employ the $\Theta_c(D_*)$ relationships empirically proposed by Cao *et al.*[37] (Appendix B). The sediment suspension prevails when the Shields number exceeds its threshold value Θ_s for the initiation of sediment suspension. The empirical relations given by van Rijn[38] are used herein to determine Θ_s (Appendix B). In essence, the bedload remains the dominant mode of sediment transport for $\Theta_c<\Theta<\Theta_s$. On the other hand, for $\Theta>\Theta_s$, both the bedload and suspended load transport prevail.

The components of bedload flux vector in s- and n-direction are expressed as[25,28]

$$\Phi_{bs}=\Phi\left\{\cos\chi\left[1-\frac{1}{2}\left(\frac{1}{\beta(1+\nu nBC)}\cdot\frac{\partial\eta}{\partial s}\right)^2\right]-\frac{\sin\chi}{\beta^2B(1+\nu nBC)}\cdot\frac{\partial\eta}{\partial n}\cdot\frac{\partial\eta}{\partial s}\right\}, \quad (13)$$

$$\Phi_{bn}=\Phi\sin\chi\left[1-\frac{1}{2}\left(\frac{1}{\beta B}\cdot\frac{\partial\eta}{\partial n}\right)^2\right], \quad (14)$$

respectively, where η is the dimensionless local bed elevation ($=F^2H-D$), Φ is the resultant bedload flux intensity, and χ is the angle formed by the resultant bedload flux with the streamwise direction. The χ reads[25,28]

$$\chi=\sin^{-1}\left[\frac{T_n}{(T_s^2+T_n^2)^{0.5}}-\frac{\wp}{\beta B\Theta^{0.5}}\cdot\frac{\partial\eta}{\partial n}\right], \quad (15)$$

where $\wp$ is an empirical coefficient ranging from 0.5 to 0.6.[39] Literature evidences that Φ is a monotonically increasing function of the Shields number. In this formulation, we use the empirical formula of Meyer-Peter and Müller,[40]

$$\Phi=8(\Theta-\Theta_c)^{1.5}. \quad (16)$$

It is worth mentioning that Ali and Dey[41] obtained the exponent ($=1.5$) of Meyer-Peter and Müller formula from the phenomenological theory of turbulence.

To estimate the suspended load flux vector, we employ the depth-averaged model of Bolla Pittaluga and Seminara.[42] They presented a depth-averaged formulation for the suspended load flux vector in slowly varying flows based on the asymptotic expansion of the exact solution of the advection-diffusion equation of sediment concentration. They considered that the advective and unsteady effects are negligible as compared to the gravitational settling and turbulent diffusion. This mathematically reads

$$\delta_a=\frac{U_0^*D_0^*}{w_s^*\lambda^*}\ll 1, \quad (17)$$

where w_s^* is the terminal fall velocity of sediment particles and λ^* is the meander wavelength. To determine w_s^*, we employ the empirical relation of Jiménez and Madsen (see Appendix B).[43] It is apparent that δ_a depends on the priori unknown λ^*. Hence, we consider another small parameter δ_k as[44–47]

$$\delta_k=\delta_a\frac{\lambda^*}{B_0^*}=\frac{U_0^*}{\beta w_s^*}. \quad (18)$$

The suspended load flux vector reads[42]

$$(\Phi_{ss}, \Phi_{sn})=D(U_s, U_n)\psi, \quad (19)$$

where ψ is a function that can be expended as $\psi=\psi_0+\delta_k\psi_1+O(\delta_k^2)$. Here, ψ_0 defines the function under the uniform flow condition and ψ_1 takes into account the weak nonequilibrium effects owing to the spatial variation of the flow field. The ψ_0 and ψ_1 are expressed as[42,44]

$$\psi_0 = \xi_0 K_0, \quad \psi_1 = K_1 D\left[\frac{U_s}{(1+\nu n B C)}\cdot\frac{\partial \xi_0}{\partial s} + \frac{U_n}{B}\cdot\frac{\partial \xi_0}{\partial n}\right], \tag{20}$$

where ξ_0 is the depth-averaged suspended sediment concentration, and K_0 and K_1 are the functions of pertinent physical parameters. The ξ_0 is expressed as[44]

$$\xi_0 = \frac{1}{1-a}\xi_a J_1 \quad \text{with} \quad J_1 = \int_a^1 \left(\frac{a}{1-a}\cdot\frac{1-z}{z}\right)^{\zeta} \mathrm{d}z, \tag{21}$$

where $a = a^*/D_0^*$, $z = z^*/D_0^*$, a^* is the reference level, which demarcates the bedload and suspended load transport, ξ_a is the reference concentration, ζ is the Rouse number $[= w_s^* S_c/(\kappa u_f^*)]$, S_c is the turbulent Schmidt number ($\approx$1), and κ is the von Kármán coefficient ($\approx$0.41). To estimate a and ξ_a, we use the empirical relations of van Rijn (see Appendix B).[38] The function K_0 appearing in Eq. (20) reads[44]

$$K_0 = \frac{C_f^{0.5}}{\kappa}(1-a)\left(\frac{J_2}{J_1} + K_2\right). \tag{22}$$

In the above, K_2 and J_2 are defined as[44]

$$K_2 = 0.777 + \frac{\kappa}{C_f^{0.5}}$$

and

$$J_2 = \int_a^1 (\ln z + 1.84z^2 - 1.56z^3)\left(\frac{a}{1-a}\cdot\frac{1-z}{z}\right)^{\zeta} \mathrm{d}z. \tag{23}$$

The function K_1 in Eq. (20) is expressed as[42,44]

$$K_1 = \frac{C_f^{0.5}}{\kappa}\left[\int_a^1 \xi_{12}(\ln z + 1.84z^2 - 1.56z^3)\mathrm{d}z - \ln z_0 \int_a^1 \xi_{12}\mathrm{d}z\right], \tag{24}$$

where ξ_{12} is a function and z_0 is dimensionless zero-velocity level $(= z_0^*/D_0^*)$. To determine ξ_{12}, we solve the following differential equation subject to the boundary conditions: $\partial\xi_{12}/\partial z = 0$ at $z = a$ and $\xi_{12} = 0$ at $z = 1$:[42]

$$\frac{\partial \xi_{12}}{\partial z} + \zeta^{-1}\frac{\partial}{\partial z}\left[z(1-z)\frac{\partial}{\partial z}\right]\xi_{12} = \frac{(1-a)C_f^{0.5}}{\kappa J_1}\left(\ln\frac{z}{z_0} + 1.84z^2 - 1.56z^3\right)\left(\frac{a}{1-a}\cdot\frac{1-z}{z}\right)^{\zeta}. \tag{25}$$

Finally, we consider that the channel banks are impermeable to flow and sediment fluxes. This mathematically reads[25,26,28]

$$\left(U_n - U_s\frac{\partial B}{\partial s}\right)\Big|_{n=\pm1} = \left(\Phi_{bn} - \Phi_{bs}\frac{\partial B}{\partial s}\right)\Big|_{n=\pm1} = \left(\Phi_{sn} - \Phi_{ss}\frac{\partial B}{\partial s}\right)\Big|_{n=\pm1} = 0. \tag{26}$$

III. PERTURBATION SOLUTION

We consider a regular sine-generated meander with curvature and width oscillations as follows:[28]

$$C(s) = C_1 e_1 + C_3 e_3 + \text{c.c.} \quad \text{and} \quad b(s) = b_2 e_2 + \text{c.c.}, \tag{27}$$

where C_1, C_3, and b_2 are the complex constants, and c.c. represents the complex conjugate. In Eq. (27), $e_m = \exp(imks)$ with $m = 1$ to 3, where mk is the dimensionless meander wavenumber associated with the mth harmonic and i denotes the imaginary unit $[= (-1)^{0.5}]$. It is important to mention that the width variation is considered to be in phase with the channel curvature. We expand the pertinent variables in terms of ν and δ as[28]

$$\begin{aligned}\boldsymbol{V} = \boldsymbol{V}_0 &+ \nu(\boldsymbol{V}_{10}^1 C_1 e_1 + \boldsymbol{V}_{10}^3 C_3 e_3 + \text{c.c.}) + \delta(\boldsymbol{V}_{01}^2 b_2 e_2 + \text{c.c.}) \\ &+ \nu^2(\boldsymbol{V}_{20}^2 C_1^2 e_2 + \text{c.c.}) + \nu\delta(\boldsymbol{V}_{11}^1 \bar{C}_1 b_2 e_1 + \boldsymbol{V}_{11}^3 C_1 b_2 e_3 + \text{c.c.}),\end{aligned} \tag{28}$$

where $\boldsymbol{V} = (U_s, U_n, H, D)^{\mathrm{T}}$, $\boldsymbol{V}_0 = (1, 0, H_0, 1)^{\mathrm{T}}$, $\boldsymbol{V}_{ij}^m = (U_{sij}^m, U_{nij}^m, H_{ij}^m, D_{ij}^m)^{\mathrm{T}}$; subscripts (i, j) are (1, 0), (0, 1), (2, 0), and (1, 1) at orders ν, δ, ν^2, and $\nu\delta$, respectively (in subsequent text also); superscript m (1 to 3) refers to the mth harmonic at any order of perturbation expansion (in subsequent text also); and overbar denotes the conjugate of a complex number. The bed shear stress and sediment flux vectors are also expended. Substituting Eqs. (27) and (28) into Eqs. (4)–(7), we obtain a set of ordinary differential equation for all unknowns at each order of perturbation expansion as follows:

$$(imk + \beta t_1 C_{f0})U_{sij}^m + imkH_{ij}^m + \beta C_{f0}(t_2 - 1)D_{ij}^m = f_{1ij}^m, \tag{29}$$

$$\frac{\mathrm{d}H_{ij}^m}{\mathrm{d}n} + (imk + \beta C_{f0})U_{nij}^m = f_{2ij}^m, \tag{30}$$

$$\frac{\mathrm{d}U_{nij}^m}{\mathrm{d}n} + imk(U_{sij}^m + D_{ij}^m) = f_{3ij}^m, \tag{31}$$

$$\begin{aligned}&\left(\gamma\Phi_0 + \frac{\psi_{00}}{1-p}\right)\frac{\mathrm{d}U_{nij}^m}{\mathrm{d}n} + \left\{imkt_3\gamma\Phi_0 + \frac{\psi_{00}}{1-p}\left[imk(1+t_5) - \delta_k m^2 k^2 t_7\right]\right\}U_{sij}^m \\ &\frac{\gamma\Phi_0\wp}{\beta\Theta_0^{0.5}}\left(\frac{\mathrm{d}^2 D_{ij}^m}{\mathrm{d}n^2} - F^2\frac{\mathrm{d}^2 H_{ij}^m}{\mathrm{d}n^2}\right) + \left\{imkt_4\gamma\Phi_0 + \frac{\psi_{00}}{1-p}\left[imk(1+t_6) - \delta_k m^2 k^2 t_8\right]\right\}D_{sij}^m = f_{4ij}^m,\end{aligned} \tag{32}$$

where C_{f0}, Φ_0, and Θ_0 are the unperturbed friction coefficient, bedload flux intensity, and Shields number, respectively, t_{1-8} are the coefficients given in Appendix C, and f_{rij}^m $(r = 1$ to 4) are the complex forcing terms owing to the curvature and width variations. Using Eqs. (29)–(32), we obtain the fourth-order linear ordinary differential equation for the radial velocity perturbation at any order,

$$\frac{\mathrm{d}^4 U_{nij}^m}{\mathrm{d}n^4} + \Im_{1ij}^m\frac{\mathrm{d}^2 U_{nij}^m}{\mathrm{d}n^2} + \Im_{2ij}^m U_{nij}^m = \Im_{3ij}^m. \tag{33}$$

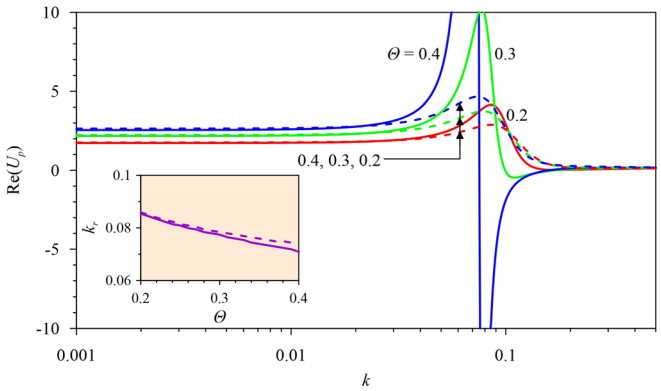

FIG. 3. Re(U_p) vs k for $d_s = 0.005$, $\beta = 20$, $\delta = 0.1$, $R_* = 100$ and different values of Θ (solid and dashed lines correspond to the results with and without sediment suspension, respectively).

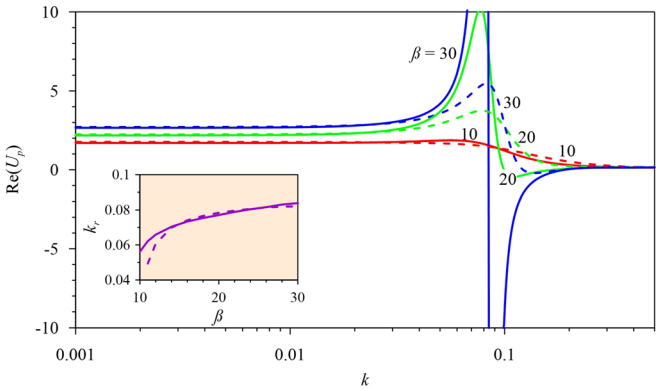

FIG. 5. Re(U_p) vs k for $\Theta = 0.3$, $d_s = 0.005$, $\delta = 0.1$, $R_* = 100$ and different values of β (solid and dashed lines correspond to the results with and without sediment suspension, respectively).

The above differential problem is associated with the following boundary conditions:

$$\left(U^m_{nij}, \frac{\mathrm{d}^2 U^m_{nij}}{\mathrm{d}n^2}\right)\Big|_{n=\pm 1} = \pm(\Im^m_{4ij}, \Im^m_{5ij}). \tag{34}$$

In Eqs. (33) and (34), $\Im^m_{qij}$ ($q = 1$ to 5) are the coefficients depending on relevant physical conditions. The solution of Eq. (33) provides the radial velocity perturbation at each order. Finally, substituting the radial velocity perturbations in Eqs. (29)–(31), the azimuthal velocity perturbation and the bed topography perturbation can be obtained.

IV. RESULTS AND DISCUSSION

It is recognized that only the laterally anti-symmetrical perturbation of the azimuthal velocity with the fundamental longitudinal frequency is linked with the bend instability.[25] We find that solutions at orders $O(\nu)$ and $O(\nu\delta)$ are anti-symmetrical. Hence, we study the behavior of the excess azimuthal velocity U_p ($= U^1_{s10} + \delta U^1_{s11}$) with dimensionless meander wavenumber k on a semi-logarithmic scale (Figs. 3–7). The theoretical analysis reveals that the U_p depends on the Shields number Θ, relative roughness number d_s ($= d^*/D^*_0$), channel aspect ratio β, width-variation amplitude δ, and shear Reynolds number R_*.

Figure 3 presents the variations of the real part of excess azimuthal velocity Re(U_p) with dimensionless meander wavenumber k for different Shields numbers Θ. The solid and dashed lines describe the results with and without sediment suspension, respectively (also in subsequent Figs. 4–12). Note that the results are obtained at the channel outer bank ($n = 1$). It is apparent from Fig. 3 that for a given Θ, Re(U_p) does not vary significantly with k for $k < 0.03$ and $k > 0.2$. For intermediate wavenumbers with $\Theta = 0.2$, 0.3, and 0.4 (without sediment suspension) and $\Theta = 0.2$ (with sediment suspension), the Re(U_p) increases with an increase in k reaching the maximum value, and then diminishes to become a constant for $k > 0.2$. In the intermediate wavenumber range for $\Theta = 0.3$ and 0.4 (with sediment suspension), Re(U_p) amplifies with k attaining a positive peak, and thereafter decreases to a minimum. Subsequently, the Re(U_p) dampens as the k increases to become independent of k for $k > 0.2$. The positive peaks of Re(U_p)(k) curves appear to be sensitive to the Shields number. An increase in Shields number signifies a decrease in particle size with an enhanced sediment suspension. With an increase in Θ, the positive

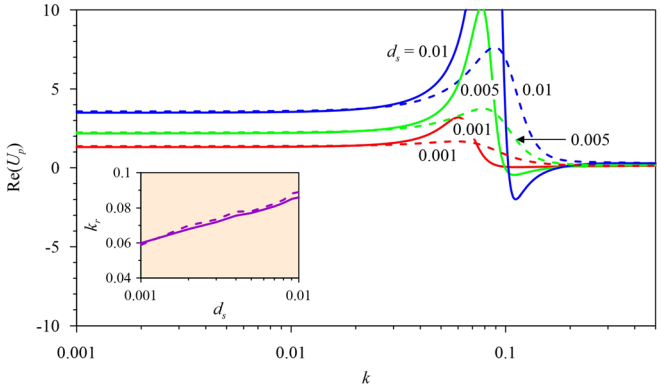

FIG. 4. Re(U_p) vs k for $\Theta = 0.3$, $\beta = 20$, $\delta = 0.1$, $R_* = 100$ and different values of d_s (solid and dashed lines correspond to the results with and without sediment suspension, respectively).

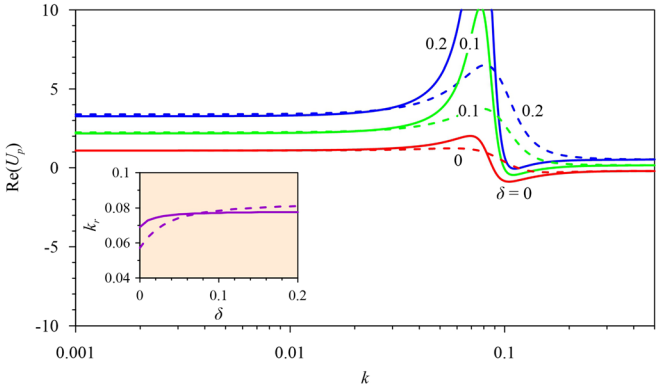

FIG. 6. Re(U_p) vs k for $\Theta = 0.3$, $d_s = 0.005$, $\beta = 20$, $R_* = 100$ and different values of δ (solid and dashed lines correspond to the results with and without sediment suspension, respectively).

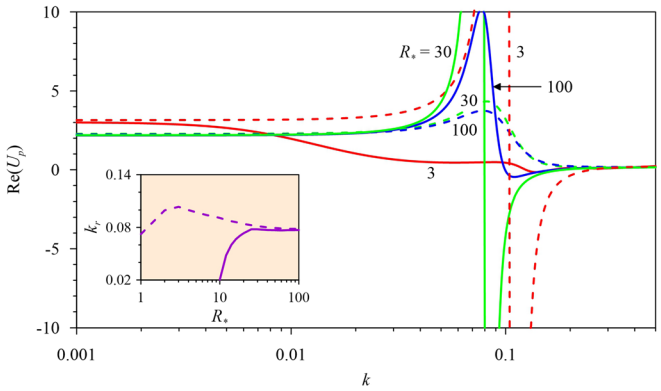

FIG. 7. Re(U_p) vs k for $\Theta = 0.3$, $d_s = 0.005$, $\beta = 20$, $\delta = 0.1$ and different values of R_* (solid and dashed lines correspond to the results with and without sediment suspension, respectively).

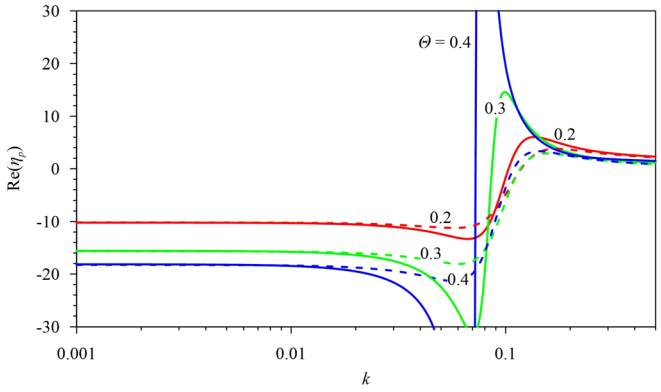

FIG. 8. Re(η_p) vs k for $d_s = 0.005$, $\beta = 20$, $\delta = 0.1$, $R_* = 100$ and different values of Θ (solid and dashed lines correspond to the results with and without sediment suspension, respectively).

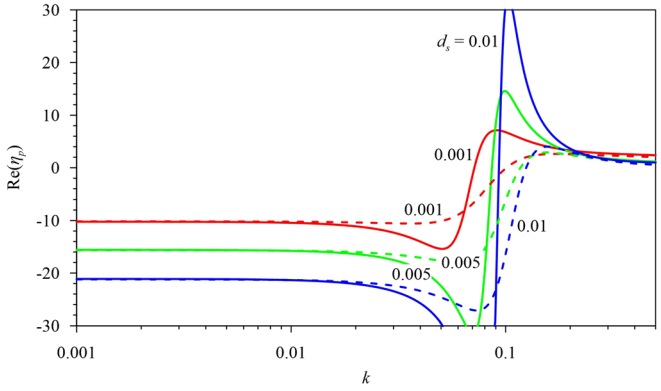

FIG. 9. Re(η_p) vs k for $\Theta = 0.3$, $\beta = 20$, $\delta = 0.1$, $R_* = 100$ and different values of d_s (solid and dashed lines correspond to the results with and without sediment suspension, respectively).

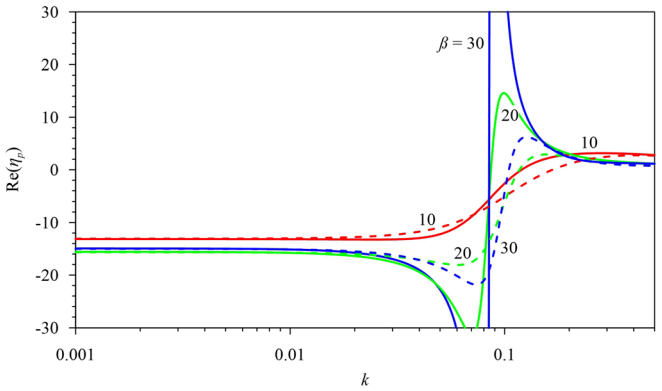

FIG. 10. Re(η_p) vs k for $\Theta = 0.3$, $d_s = 0.005$, $\delta = 0.1$, $R_* = 100$ and different values of β (solid and dashed lines correspond to the results with and without sediment suspension, respectively).

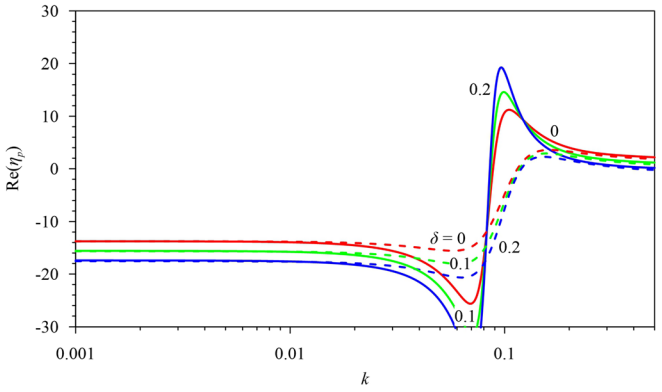

FIG. 11. Re(η_p) vs k for $\Theta = 0.3$, $d_s = 0.005$, $\beta = 20$, $R_* = 100$ and different values of δ (solid and dashed lines correspond to the results with and without sediment suspension, respectively).

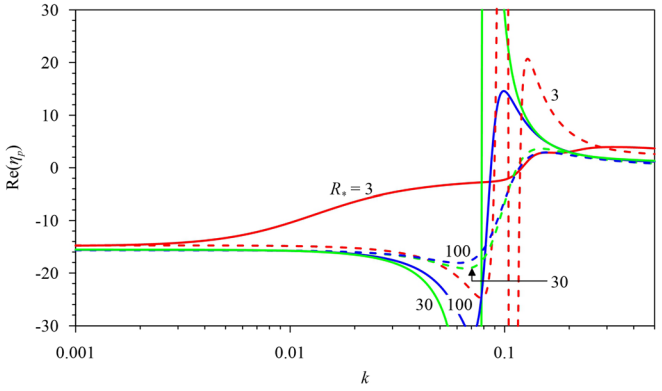

FIG. 12. Re(η_p) vs k for $\Theta = 0.3$, $d_s = 0.005$, $\beta = 20$, $\delta = 0.1$ and different values of R_* (solid and dashed lines correspond to the results with and without sediment suspension, respectively).

peak of Re(U_p)(k) curve increases. Therefore, a reduction in particle size seems to play destabilizing role toward the bend instability. The inclusion of sediment suspension leads to a higher value of the positive peak of the Re(U_p)(k) curves. Hence, we conclude that the sediment suspension plays a destabilizing role in governing the bend instability. It is also discernible that the Re(U_p)(k) curves with and without sediment suspension almost overlap for smaller ($k < 0.03$) and larger wavenumbers ($k > 0.2$). Therefore, it appears that the effects of sediment suspension are important in the intermediate wavenumber range. For each Θ, a resonance phenomenon takes place. The resonance is associated with the positive peak of the Re(U_p)(k) curve. It is interesting to explore the dimensionless wavenumber corresponding to the positive peak of the Re(U_p)(k) curve, called the *resonant wavenumber* k_r. The $k_r(\Theta)$ curves are shown in the inset of Fig. 3. The $k_r(\Theta)$ curves with and without sediment suspension exhibit similar trend. The k_r monotonically decreases with an increase in Θ. Moreover, for a given Θ, the k_r without sediment suspension possesses a higher magnitude than that with sediment suspension. Therefore, the inclusion of sediment suspension shifts the resonance toward smaller wavenumbers.

Figure 4 furnishes the variations of the Re(U_p) with k for different relative roughness numbers d_s. As the Θ and R_* are kept constant, an increase in d_s indicates a decrease in flow depth. Akin to Fig. 3, for a given d_s, the Re(U_p)(k) curves remain nearly invariant with k for $k < 0.03$ and $k > 0.2$. For the Re(U_p)(k) curves with sediment suspension, the Re(U_p) in the intermediate meander wavenumber range increases with an increase in k reaching a positive peak and then decreases to gain a minimum value. Thereafter, the Re(U_p) increases (i.e., reduction in absolute negative magnitude) with k attaining a constant magnitude for $k > 0.2$. In the intermediate wavenumber range, the behavior of Re(U_p)(k) curves without sediment suspension is somewhat different. In this case, the Re(U_p) increases with k and then diminishes reaching a constant magnitude for $k > 0.2$. It is evident that for a given d_s, the Re(U_p)(k) curves display the resonance phenomenon. The positive peak value of the Re(U_p)(k) curve amplifies as the d_s increases. Hence, a reduction in the flow depth plays a destabilizing role. It is also apparent that for a given d_s, the Re(U_p)(k) curve with sediment suspension comprises a higher positive peak. This observation ensures the destabilizing role of the sediment suspension. The $k_r(d_s)$ curves are shown in the inset of Fig. 4. The k_r monotonically increases with an increase in d_s. This suggests that a reduction in flow depth is to shift the resonance toward larger wavenumbers. It is worth mentioning that this finding accords with the previous studies of Seminara and Tubino[8] and Ali and Dey.[23] It is also explicit that the $k_r(d_s)$ curve with sediment suspension lies somewhat below the $k_r(d_s)$ curve without sediment suspension. Hence, the inclusion of sediment suspension causes the resonance to shift toward smaller wavenumbers.

The variations of the Re(U_p) with k for different channel aspect ratios β are displayed in Fig. 5. It is obvious that for $k < 0.03$ and $k > 0.3$, the Re(U_p) remains almost independent of k. In the intermediate wavenumber range, for $\beta = 10$ with sediment suspension and $\beta = 10$ and 20 without sediment suspension, the Re(U_p) amplifies with an increase in k to attain a positive peak. Then, it decreases to a constant value for $k > 0.3$. In the intermediate wavenumber range, the Re(U_p) for $\beta = 20$ and 30 (with sediment suspension) and $\beta = 30$ (without sediment suspension) increases with an increase in k to attain a positive peak and then reduces with a further increase in k to attain a minimum value. Afterward, the Re(U_p) again increases (i.e., reduction in absolute negative magnitude) with k attaining a constant magnitude for $k > 0.3$. For a given β, the positive peak value of the Re(U_p)(k) curve with sediment suspension always remains higher than that without sediment suspension. This encapsulates the destabilizing nature of sediment suspension. The $k_r(\beta)$ curves are furnished in the inset of Fig. 5. The k_r monotonically increases as the β increases. The trend of $k_r(\beta)$ agrees with the study of Ali and Dey.[23] The $k_r(\beta)$ curve with sediment suspension lies above that without sediment suspension for $\beta < 15$ and $\beta > 25$. The reverse is true for $15 < \beta < 25$. Hence, the inclusion of sediment suspension relocates the resonance toward larger wavenumbers for $\beta < 15$ and $\beta > 25$. On the contrary, for $15 < \beta < 25$, the effects of sediment suspension are to shift the resonance toward smaller wavenumbers.

Figure 6 shows the variations of the Re(U_p) with k for different width-variation amplitudes δ. For a given δ, the Re(U_p) remains almost constant with k for $k < 0.03$ and $k > 0.3$. For intermediate wavenumbers, the Re(U_p) with sediment suspension enhances with an increase in k reaching a positive peak and thereafter diminishes to attain a minimum value. Then, the Re(U_p) again grows to reach a near constant magnitude for $k > 0.3$. The behavior of Re(U_p)(k) curves without sediment suspension is slightly different. In the intermediate wavenumber range, the Re(U_p) without sediment suspension increases with k to reach a positive peak. Thereafter, the Re(U_p) decays with k and becomes invariant with k for $k > 0.3$. The positive peaks of Re(U_p)(k) curves with sediment suspension remain higher than those without sediment suspension. This observation reflects the destabilizing role of sediment suspension. Note that the Re(U_p)(k) curves with $\delta = 0$ correspond to a constant channel width. For a given k, the Re(U_p) amplifies as the δ increases. Hence, the width variation favors the bend instability. This observation is consistent with the study of Luchi *et al.*[25] The $k_r(\delta)$ curves are shown in the inset of Fig. 6. The $k_r(\delta)$ curve with sediment suspension grows with an increase in δ for $\delta < 0.04$. However, it eventually becomes a constant for $\delta > 0.04$. On the other hand, the $k_r(\delta)$ curve without sediment suspension grows as the δ increases. For $\delta < 0.08$, the $k_r(\delta)$ curve with sediment suspension remains above that without sediment suspension, while the reverse scenario takes place for $\delta > 0.08$. The sediment suspension causes to shift the resonance toward larger and smaller wavenumbers for $\delta < 0.08$ and $\delta > 0.08$, respectively.

It is interesting to explore the behavior of Re(U_p) in different flow regimes. To this end, Fig. 7 displays the Re(U_p)(k) curves in hydraulically smooth ($R_* = 3$), transitional ($R_* = 30$), and rough ($R_* = 100$) flow regimes. In a hydraulically smooth flow regime ($R_* = 3$), the Re(U_p) with sediment suspension decays with k for $k < 0.07$, while it remains almost constant for $k > 0.3$. For intermediate wavenumbers, the Re(U_p) with sediment suspension grows with an increase in k to attain a local maximum value and then diminishes to reach a minimum value. Eventually, it attains a constant value for $k > 0.3$. The Re(U_p) without sediment suspension remains almost independent of k for $k < 0.01$ and $k > 0.3$. In addition, for intermediate wavenumbers, the Re(U_p) increases with an increase in k reaching a positive peak and then reduces with k to attain a minimum value. Thereafter, it becomes independent of k for $k > 0.3$. In hydraulically transitional ($R_* = 30$) and rough ($R_* = 100$) flow regimes, the Re(U_p)(k) curves are nearly identical. The Re(U_p) remains independent of k for $k < 0.01$ and $k > 0.3$. In the intermediate wavenumber range for $R_* = 30$ and 100,

the $\mathrm{Re}(U_p)$ with sediment suspension amplifies with an increase in k to attain a positive peak. Thereafter, it reduces with k to reach a minimum value and eventually grows with further increase in k to become independent of k for $k > 0.3$. For $R_* = 30$ and 100, the $\mathrm{Re}(U_p)$ without sediment suspension in the intermediate wavenumber range enhances with an increase in k attaining a positive peak and finally diminishes with a further increase in k to become a constant for $k > 0.3$. For $R_* = 30$ and 100, the positive peak of the $\mathrm{Re}(U_p)(k)$ curve amplifies with the inclusion of sediment suspension. On the contrary, for $R_* = 3$, the positive peak of the $\mathrm{Re}(U_p)(k)$ curve diminishes with the inclusion of sediment suspension. Hence, the sediment suspension plays a destabilizing role in hydraulically transitional and rough flow regimes, while it plays as a stabilizing role in a hydraulically smooth flow regime. The $k_r(R_*)$ curves are shown in the inset in Fig. 7. The k_r with sediment suspension increases with an increase in R_* for $R_* < 25$ remaining independent of R_* for $R_* > 25$. On the other hand, the k_r without sediment suspension grows with R_* attaining a maximum at $R_* = 3$. Thereafter, it lessens with a further increase in R_*. The $k_r(R_*)$ curve without sediment suspension stays above that with sediment suspension. Hence, the sediment suspension tends to shift the resonance toward smaller wavenumbers.

The evolution of bed topography has been studied extensively in the field of morphodynamics.[14,24,48] It is worth noting that the solutions at orders ν and $\nu\delta$ are associated with the anti-symmetric pattern of bed topography. Hence, we study the behavior of bed topography deviation $\eta_p\ (= \eta^1_{10} + \delta\eta^1_{11})$ with dimensionless meander wavenumber k, where $\eta^1_{10} = F^2H^1_{10} - D^1_{10}$ and $\eta^1_{11} = F^2H^1_{11} - D^1_{11}$. Figure 8 displays the variations of the real part of bed topography deviation with dimensionless meander wavenumber k for different Shields numbers Θ. For a given Θ, the $\mathrm{Re}(\eta_p)$ remains independent of k for $k < 0.01$. For $k > 0.01$, the $\mathrm{Re}(\eta_p)$ decreases with an increase in k to attain a negative peak. Thereafter, it increases (i.e., reduction in absolute negative magnitude) with a further increase in k to reach a positive peak. Afterward, the $\mathrm{Re}(\eta_p)$ decreases with k. It is apparent that an increase in Θ causes to amplify the magnitude of positive and negative peaks. Hence, a reduction in sediment particle size destabilizes the process of bend instability. It is also evident that the positive and negative peaks of the $\mathrm{Re}(\eta_p)(k)$ curves with sediment suspension possess higher magnitudes as compared to those without sediment suspension. Note that an increase in Θ causes to shift the resonance toward smaller wavenumbers.

The variations of the $\mathrm{Re}(\eta_p)$ with k for different relative roughness numbers d_s are shown in Fig. 9. For a given d_s, the behavior of $\mathrm{Re}(\eta_p)(k)$ curves are similar to those in Fig. 8. For a given Θ and R_*, an increase in d_s represents a reduction in flow depth. It is noticeable that the positive and negative peaks of $\mathrm{Re}(\eta_p)(k)$ curves amplify as the d_s increases. Hence, a decrease in flow depth destabilizes the bend instability. It also appears that an increase in d_s causes the resonance toward larger wavenumbers.

Figure 10 furnishes the $\mathrm{Re}(\eta_p)(k)$ curves for different channel aspect ratios β. For a given β, the $\mathrm{Re}(\eta_p)$ is independent of k for $k < 0.01$. For $k > 0.01$ with $\beta = 10$, the $\mathrm{Re}(\eta_p)$ grows with an increase in k and eventually becomes constant for $k > 0.3$. On the other hand, for $k > 0.01$ with $\beta = 20$ and 30, the $\mathrm{Re}(\eta_p)$ diminishes with an increase in k to reach a negative peak. Subsequently, it grows with a further increase in k to attain a positive peak. Afterward, the $\mathrm{Re}(\eta_p)$ decays with k. The $\mathrm{Re}(\eta_p)$ enhances with the channel aspect ratio. Akin to Figs. 8 and 9, the destabilizing role of sediment suspension is apparent.

The $\mathrm{Re}(\eta_p)(k)$ curves for different width-variation amplitudes δ are depicted in Fig. 11. For a given δ, the trend of $\mathrm{Re}(\eta_p)(k)$ curves is similar to those in Figs. 8 and 9. The positive and negative peaks of the $\mathrm{Re}(\eta_p)(k)$ curves with sediment suspension amplify as the δ increases. On the other hand, for the $\mathrm{Re}(\eta_p)(k)$ curves without sediment suspension, an increase in δ causes the amplification and decay of negative and positive peaks, respectively. Note that the curves with $\delta = 0$ represent the bed topography deviation for a constant channel width. Note that the width variation strengthens the bend instability.

In Fig. 12, the variations of the $\mathrm{Re}(\eta_p)$ with k in different flow regimes are shown. In a hydraulically smooth flow regime ($R_* = 3$) with sediment suspension, the $\mathrm{Re}(\eta_p)$ increases with an increase in k for $k < 0.07$. Then, it slowly diminishes with k to attain a local minimum value. Thereafter, it increases with a further increase in k becoming independent of k for $k > 0.3$. For $R_* = 3$ without sediment suspension, the $\mathrm{Re}(\eta_p)$ remains almost independent of k for $k < 0.01$. Then, it decreases with an increase in k to reach a local minimum value. Thereafter, it abruptly amplifies and decays with an increase in k to attain positive and negative peaks, respectively. Afterward, it increases with a further increase in k to reach a local maximum value and finally decays with k. Note that in hydraulically transitional ($R_* = 30$) and rough ($R_* = 100$) flow regimes, the $\mathrm{Re}(\eta_p)$ is almost invariant with k for $k < 0.01$. Akin to Fig. 7, the stabilizing role of sediment suspension is evident in a hydraulically smooth flow regime. In addition, in hydraulically transitional and rough flow regimes, the destabilizing nature of sediment suspension is apparent.

Figure 13 shows the variations of the dimensionless resonant wavenumber k_r with channel aspect ratio β. The $k_r(\beta)$ curves of several investigators are also plotted for the comparison. To make the comparison in Fig. 13, the $k_r(\beta)$ curve of this study is obtained by neglecting the effects of sediment suspension and width variation. The trend of the $k_r(\beta)$ curve of this study agrees well with those of Blondeaux and Seminara[4] and Ali and Dey.[23] However, for a given β, this study underpredicts the k_r. This may be attributed to the precise estimation of the radial bed shear stress. Note that the $k_r(\beta)$ curves of Ikeda *et al.*[2] and Kitiandis and Kennedy[49] overpredict the k_r, because the resonance was not identified in their studies.

An enhanced understanding of the bend instability can be obtained from the stability diagrams of the excess azimuthal velocity.

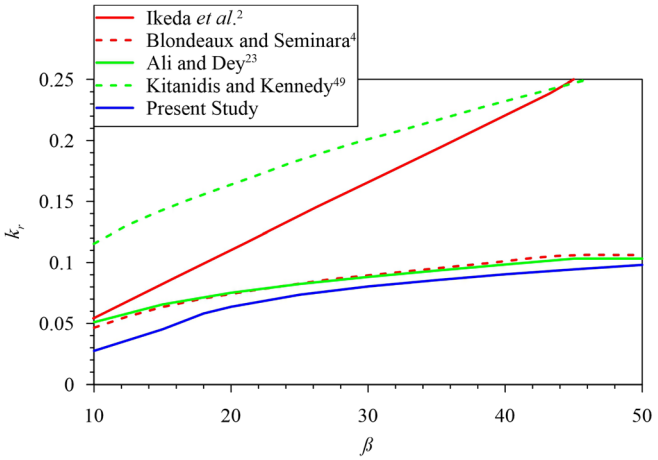

FIG. 13. K_r vs β for $\Theta = 0.3$, $d_s = 0.005$, $R_* = 100$, and $\delta = 0$.

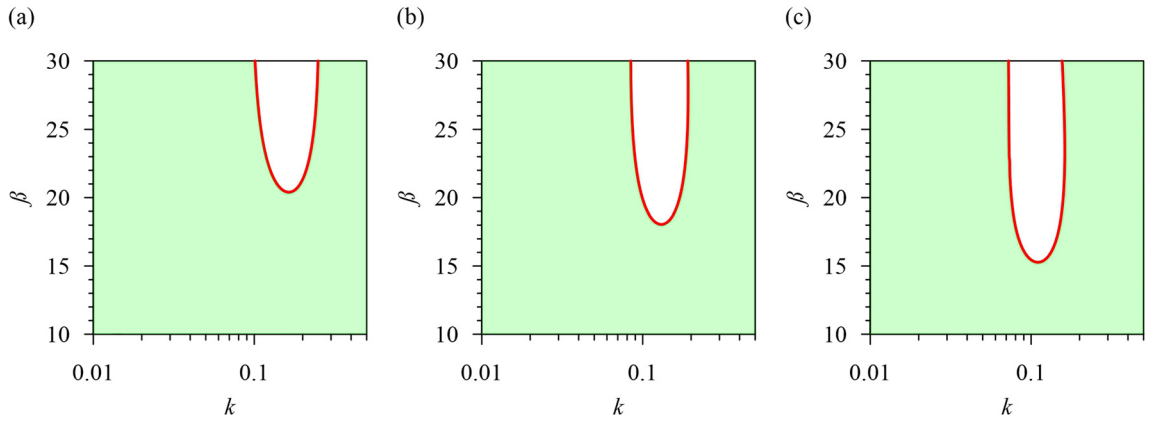

FIG. 14. Stability diagrams for $d_s = 0.005$, $\delta = 0.1$, and $R_* = 100$: (a) $\Theta = 0.2$, (b) $\Theta = 0.3$, and (c) $\Theta = 0.4$ (shaded and white areas represent the unstable and stable zones, respectively).

Figures 14–18 furnish the stability diagrams on the $\beta(k)$ plane. In natural channels, sediment is transported as both bedload and suspended load. Hence, the stability diagrams in Figs. 14–17 are obtained considering the effects of sediment suspension in addition to the bedload, while Fig. 18 is obtained considering sediment transport as bedload only. The stability diagram comprises the stable $[\mathrm{Re}(U_p) < 0]$ and unstable $[\mathrm{Re}(U_p) > 0]$ zones.

Figures 14(a)–14(c) display the stability diagrams for different Shields numbers Θ. The shaded and white zones denote the unstable and stable zones, respectively (also in Figs. 15–17). The red line indicates the neutral stability condition (also in Figs. 15–17). The stable zone expands with an increase in Θ (i.e., decrease in particle size). A close inspection of Fig. 14 reveals that an increase in Θ destabilizes larger wavenumbers. This is in agreement with the study of Luchi *et al.*[25] The stable zone exists beyond a critical channel aspect ratio β_k. It is apparent that the β_k reduces as the Θ increases. In Figs. 15(a)–15(c), the stability diagrams are furnished for different relative roughness numbers d_s. An increase in d_s stabilizes the larger wavenumbers. Moreover, with an increase in d_s, the β_k reduces. Figures 16(a)–16(c) depict the stability diagrams for different width-variation amplitudes δ. The stable zone shrinks significantly as the δ increases. The β_k increases with an increase in δ.

Figures 17(a)–17(c) show the stability diagrams in hydraulically smooth ($R_* = 3$), transitional ($R_* = 30$), and rough ($R_* = 100$) flow regimes, respectively. In a hydraulically smooth flow regime, three separate stable zones appear. The stable zones appear to move toward larger wavenumbers as the β increases. Note that the concept of β_k breaks down in the stability diagram for $R_* = 3$. In hydraulically transitional ($R_* = 30$) and rough ($R_* = 100$) flow regimes, the stability diagrams characterize a unique stable zone. The stable zone for $R_* = 100$ appears to be smaller than that for $R_* = 30$. In addition, the β_k for $R_* = 100$ is larger than that for $R_* = 30$.

The sensitivity of the stability diagrams to the effects of sediment suspension is not apparent in Figs. 14–17. To this end, Fig. 18 depicts the stability diagrams with and without sediment suspension. The solid and dashed lines denote the neutral stability curves with and without sediment suspension, respectively. The interior and exterior zones of a given curve indicate the stable and unstable zones, respectively. The inclusion of sediment suspension (solid line) causes the stable zone to amplify. Moreover, the stable zone is slightly shifted toward

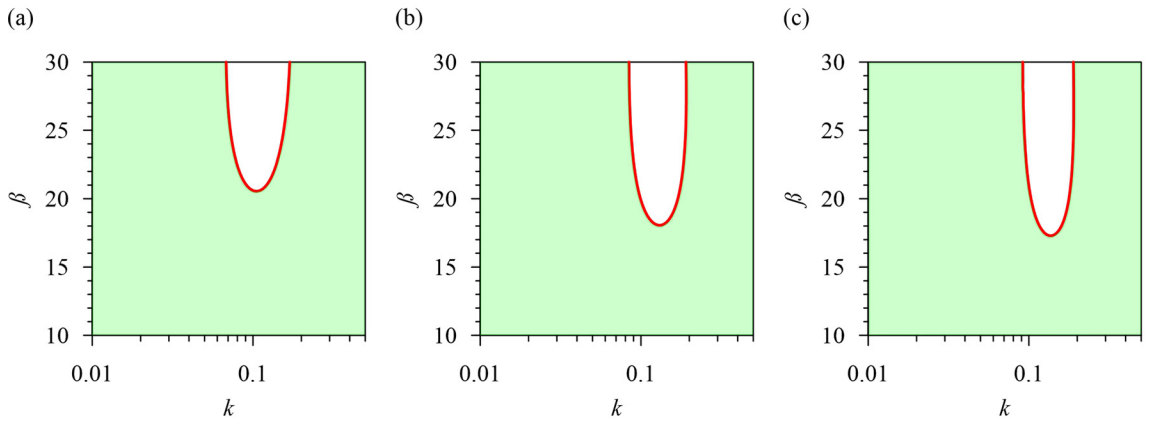

FIG. 15. Stability diagrams for $\Theta = 0.3$, $\delta = 0.1$, and $R_* = 100$: (a) $d_s = 0.001$, (b) $d_s = 0.005$, and (c) $d_s = 0.01$ (shaded and white areas represent the unstable and stable zones, respectively).

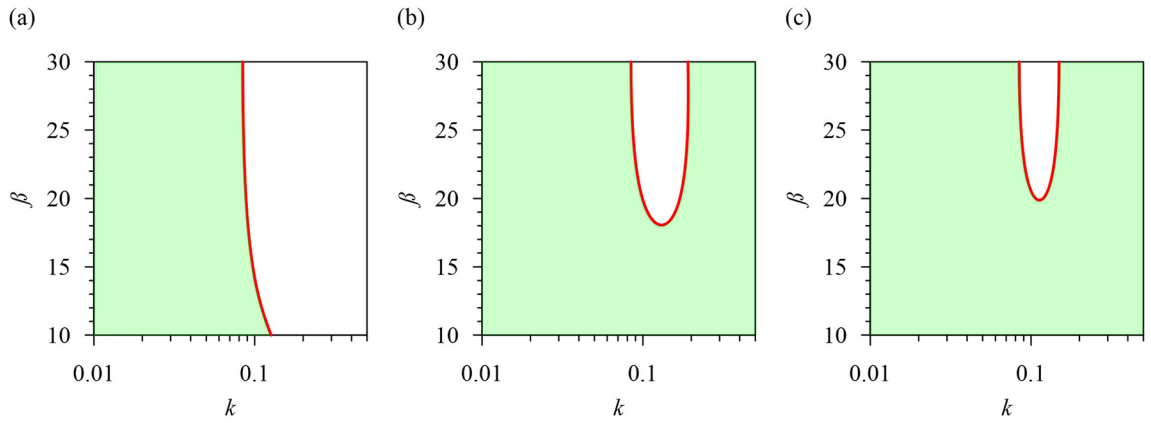

FIG. 16. Stability diagrams for $\Theta = 0.3$, $d_s = 0.005$, and $R_* = 100$: (a) $\delta = 0$, (b) $\delta = 0.1$, and (c) $\delta = 0.2$ (shaded and white areas represent unstable and stable zones, respectively).

smaller wavenumbers. In the intermediate wavenumber range, the sediment suspension appears to stabilize a range of channel aspect ratio, and subsequently critical aspect ratio β_k reduces. This behavior is attributed to the fact that the sediment suspension amplifies (reduction in negative amplitude) the minima of the $\mathrm{Re}(U_p)(k)$ curves (see Figs. 3–6).

It is interesting to further compare the key observations of this study with those reported in the literature. The appearance of the resonance phenomenon for critical values of the relevant parameters confirms the earlier observations.[4,14,23–25] Importantly, this study discloses that the sediment suspension switches the resonance toward smaller or larger wavenumbers depending on the characteristic parameters. Moreover, the observed behavior of the resonant wavenumber with the Shields number, relative roughness number, and channel aspect ratio agrees well with the study of Ali and Dey.[23] Luchi *et al.*[25] discovered that the width variation reinforces the bend instability process. In this respect, this study corroborates the observation of Luchi *et al.*[25] In addition, for a given width variation amplitude, this study reveals that the sediment suspension further strengthens the bend instability process. It unveils that the sediment suspension plays a vital role in the intermediate wavenumber range. The stability diagrams reveal that the inclusion of sediment suspension causes to enlarge the stable zone. In particular, an increase in Shields number is found to destabilize larger wavenumbers, while an increase in relative roughness number stabilizes larger wavenumbers. These observations are in agreement with the study of Luchi *et al.*[25]

V. CONCLUSIONS

We explore the stability of a meandering channel with variable width and curvature. The analysis is performed considering both modes of sediment transport as bedload and suspended load. The variations of the near-bank excess azimuthal velocity and bed topography deviation with meander wavenumber are investigated for different values of Shields number, relative roughness number, channel aspect ratio, width-variation amplitude, and shear Reynolds number. The stability diagrams are presented on the plane formed by the channel aspect ratio and the wavenumber. The sensitivity of the stability diagrams to the pertinent parameters is also explored.

With regard to the near-bank excess azimuthal velocity, the positive peaks amplify with an increase in Shields number, relative roughness number, channel aspect ratio, and width-variation amplitude. However, they decay with an increase in shear Reynolds number when

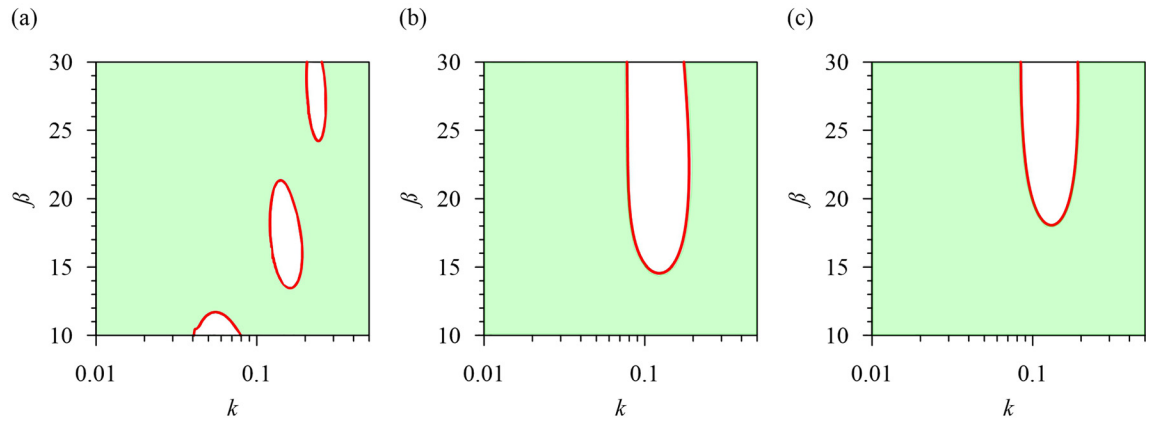

FIG. 17. Stability diagrams for $\Theta = 0.3$, $d_s = 0.005$, and $\delta = 0.1$: (a) $R_* = 3$, (b) $R_* = 30$, and (c) $R_* = 100$ (shaded and white areas represent the unstable and stable zones, respectively).

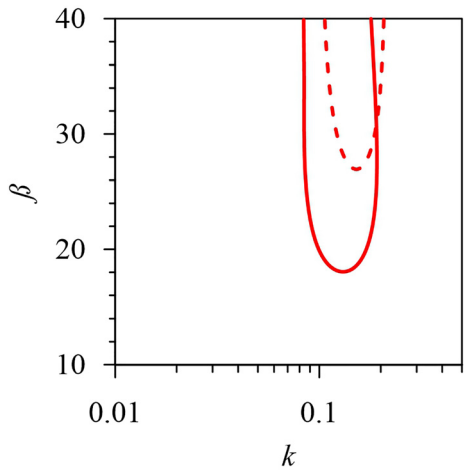

FIG. 18. Stability diagrams for $\Theta = 0.3$, $d_s = 0.005$, $\delta = 0.1$, and $R_* = 100$ (solid and dashed lines indicate the neutral stability curves with and without sediment suspension, respectively).

the sediment is transported as bedload only. It is revealed that the role of sediment suspension varies with the flow regimes. In a hydraulically smooth flow regime, the positive peak of the near-bank excess azimuthal velocity diminishes with the inclusion of sediment suspension. On the contrary, the inclusion of sediment suspension in hydraulically transitional and rough flow regimes enhances the positive peak. Hence, the sediment suspension plays a stabilizing role in a hydraulically smooth flow regime, while it plays a destabilizing role in hydraulically transitional and rough flow regimes.

An increase in Shields number switches the resonance toward smaller wavenumbers, while an increase in relative roughness number and channel aspect ratio shifts the resonance toward larger wavenumbers. With the inclusion of sediment suspension, the resonance switches toward larger wavenumbers for small and large channel aspect ratios. The resonant wavenumber increases with an increase in width-variation amplitude when the sediment is transported as bedload only. With the sediment suspension, the resonant wavenumber initially increases as the width-variation amplitude increases and eventually becomes independent of the width-variation amplitude. The sediment suspension switches the resonance toward larger and smaller wavenumbers for small and large values of width-variation amplitude, respectively. Without the sediment suspension, the resonant wavenumber increases with an increase in shear Reynolds number attaining a peak and thereafter decays with a further increase in shear Reynolds number. With the sediment suspension, the resonant wavenumber initially amplifies with shear Reynolds number and eventually attains a constant value.

The positive and negative peaks of the near-bank bed topography deviation amplify with an increase in Shields number, relative roughness number, channel aspect ratio, and width-variation amplitude. Without sediment suspension, the positive and negative peaks diminish as the shear Reynolds number increases. The sediment suspension is found to play a stabilizing role in a hydraulically smooth flow regime. On the other hand, in hydraulically transitional and rough flow regimes, the sediment suspension has a destabilizing effect.

The stability diagrams reveal that the stable zone expands with an increase in Shields number and relative roughness number. On the contrary, an increase in width-variation amplitude results in a contraction of the stable zone. In a hydraulically smooth flow regime, the stability diagram characterizes different stable zones, while in hydraulically transitional and rough flow regimes, a unique stable zone appears for a given shear Reynolds number.

In essence, the study offers insights into the role of sediment suspension in producing the instability in a meandering channel with variable width and curvature. The analysis explores the role of Shields number, relative roughness number, channel aspect ratio, width-variation amplitude, and shear Reynolds number associated with the instability process. It is worth mentioning that the precise role of sediment suspension toward the planform evolution of a meandering channel with spatial width and curvature variations remains a key aspect, which can be explored as a future scope of research.

ACKNOWLEDGMENTS

S.D. acknowledges the J C Bose Fellowship Award [Funded by DST | Science and Engineering Research Board (SERB), Grant Reference No. JCB/2018/000004] in pursuing this work.

AUTHOR DECLARATIONS

Conflict of Interest

The authors declare no conflict of interest.

DATA AVAILABILITY

The data that support the findings of this study are available from the corresponding author upon reasonable request.

APPENDIX A: FORCING TERMS

The forcing terms appearing in Eqs. (4) and (5) are as follows:

$$
\begin{aligned}
g_{10} &= -CU_sU_n - \frac{nC\beta T_s}{D} - nCU_n\frac{\partial U_s}{\partial n} - \frac{1}{D}\cdot\frac{\partial \Gamma_1}{\partial n},\\
g_{01} &= bU_n\frac{\partial U_s}{\partial n} + n\frac{\mathrm{d}b}{\mathrm{d}s}\cdot\frac{\partial H}{\partial n} + nU_s\frac{\mathrm{d}b}{\mathrm{d}s}\cdot\frac{\partial U_s}{\partial n},\\
g_{20} &= -\frac{C}{D}\left(2\Gamma_1 + n\frac{\partial \Gamma_1}{\partial n}\right), \quad g_{11} = -\frac{b}{D}\left(n\beta CT_s - \frac{\partial \Gamma_1}{\partial n}\right),\\
h_{10} &= CU_s^2 - nC\left(\frac{\beta T_n}{D} + \frac{\partial H}{\partial n} + U_n\frac{\partial U_n}{\partial n}\right) - \frac{1}{D}\left(\frac{\partial \Gamma_1}{\partial s} + 2\frac{\partial \Gamma_2}{\partial n}\right),\\
h_{01} &= b\frac{\partial H}{\partial n} + bU_n\frac{\partial U_n}{\partial n} + nU_s\frac{\mathrm{d}b}{\mathrm{d}s}\cdot\frac{\partial U_n}{\partial n},\\
h_{20} &= -\frac{2C}{D}\left(\Gamma_2 + n\frac{\partial \Gamma_2}{\partial n}\right),\\
h_{11} &= -\frac{nb\beta CT_n}{D} + \frac{2b}{D}\cdot\frac{\partial \Gamma_2}{\partial n} + \frac{n}{D}\cdot\frac{\mathrm{d}b}{\mathrm{d}s}\cdot\frac{\partial \Gamma_1}{\partial n}.
\end{aligned}
\tag{A1}
$$

In the above, Γ_1 and Γ_2 read

$$
\Gamma_1 = \frac{DU_s}{\beta C_f^{0.5}}\left[CDU_s\left(k_0 + \frac{k_2}{\beta C_f^{0.5}}\cdot\frac{\partial D}{\partial s}\right) + \frac{k_1D^2}{\beta C_f^{0.5}}\cdot\frac{\partial}{\partial s}(CU_s)\right], \tag{A2}
$$

$$
\Gamma_2 = \frac{DU_n}{\beta C_f^{0.5}}\left[CDU_s\left(k_0 + \frac{k_2}{\beta C_f^{0.5}}\cdot\frac{\partial D}{\partial s}\right) + \frac{k_1D^2}{\beta C_f^{0.5}}\cdot\frac{\partial}{\partial s}(CU_s)\right], \tag{A3}
$$

where k_0, k_1, and k_2 are the coefficients.

APPENDIX B: EMPIRICAL RELATIONS

Cao *et al.*[37] proposed the following empirical relations for the estimation of Θ_c:

$$\begin{aligned}\Theta_c(0 < D_* \le 3.52) &= 0.1414 D_*^{-0.345},\\ \Theta_c(3.52 < D_* < 43.09)&\\ &= 0.324 D_*^{-1.02}(1 + 2.04\times 10^{-5} D_*^{4.26})^{0.35},\\ \Theta_c(D_* \ge 43.09) &= 0.045.\end{aligned} \tag{B1}$$

To determine Θ_s, we use the empirical formulation of van Rijn[38] as follows:

$$\frac{u_{fs}^*}{w_s^*}(1 < D_* \le 10) = \frac{4}{D_*}, \quad \frac{u_{fs}^*}{w_s^*}(D_* > 10) = 0.4, \tag{B2}$$

where u_{fs}^* is the shear velocity at the threshold of sediment suspension. Having u_{fs}^*, the Θ_s can be estimated using Eq. (12). The empirical formula of Jiménez and Madsen[43] is employed to determine w_s^*,

$$\frac{w_s^*}{(\Delta g^* d^*)^{0.5}} = \left(0.954 + \frac{20.48}{D_*^{1.5}}\right)^{-1}. \tag{B3}$$

To estimate ξ_a and a, we employ the following empirical relations of van Rijn:[38]

$$\xi_a = 0.015\frac{d_s}{a}\left(\frac{\Theta}{\Theta_c} - 1\right)D_*^{-0.3}, \tag{B4}$$

$$a(k_s < 0.01D) = 0.01D, \quad a(k_s \ge 0.01D) = k_s. \tag{B5}$$

APPENDIX C: COEFFICIENTS T_{1-8}

The coefficients t_{1-8} read

$$\begin{aligned}t_1 &= 2\left(1 - \frac{\Theta_0}{C_{f0}}\cdot\frac{\partial C_f}{\partial \Theta}\right)^{-1}, \quad t_2 = \frac{1}{C_{f0}}\cdot\frac{\partial C_f}{\partial D}\left(1 - \frac{\Theta_0}{C_{f0}}\cdot\frac{\partial C_f}{\partial \Theta}\right)^{-1},\\ t_3 &= \frac{\Theta_0}{\Phi_0}\cdot\frac{\partial \Phi}{\partial \Theta}t_1, \quad t_4 = \frac{\Theta_0}{\Phi_0}\cdot\frac{\partial \Phi}{\partial \Theta}t_2 + \frac{1}{\Phi_0}\cdot\frac{\partial \Phi}{\partial D},\\ t_5 &= t_1\left\{\frac{\Theta_0}{2C_{f0}}\cdot\frac{\partial C_f}{\partial \Theta} + \frac{1.5\Theta_0}{\Theta_0 - \Theta_c} - 0.5(J_{20} + K_{20}J_{10})^{-1}\right.\\ &\quad\left.\times\left[\zeta_0(J_{21} + K_{20}J_{11}) + \frac{\kappa\Theta_0 J_{10}}{C_{f0}^{1.5}}\cdot\frac{\partial C_f}{\partial \Theta}\right]\right\},\\ t_6 &= t_2\left\{\frac{1}{2} - \frac{1}{t_2} + \frac{1.5\Theta_0}{\Theta_0 - \Theta_c} - 0.5(J_{20} + K_{20}J_{10})^{-1}\right.\\ &\quad\left.\times\left[\zeta_0(J_{21} + K_{20}J_{11}) + \frac{\kappa J_{10}}{C_{f0}^{0.5}}\right]\right\},\\ t_7 &= \frac{t_1\xi_{a0}K_{10}}{1-a}\left(\frac{1.5\Theta_0}{\Theta_0 - \Theta_c}J_{10} - 0.5\zeta_0 J_{11}\right),\\ t_8 &= \frac{t_2\xi_{a0}K_{10}}{1-a}\left[\left(\frac{1.5\Theta_0}{\Theta_0 - \Theta_c} - \frac{1}{t_2}\right)J_{10} - 0.5\zeta_0 J_{11}\right],\end{aligned} \tag{C1}$$

where ζ_0, ξ_{a0}, J_{10}, J_{20}, K_{10}, and K_{20} are ζ, ξ_a, J_1, J_2, K_1, and K_2 at unperturbed state, respectively. In Eq. (C1), J_{11} and J_{21} are the integral functions given as

$$J_{11} = \int_a^1 \left(\frac{a}{1-a}\cdot\frac{1-z}{z}\right)^{\zeta_0}\ln\left(\frac{a}{1-a}\cdot\frac{1-z}{z}\right)dz, \tag{C2}$$

$$J_{21} = \int_a^1 (\ln z + 1.84z^2 - 1.56z^3)\left(\frac{a}{1-a}\cdot\frac{1-z}{z}\right)^{\zeta_0} \times \ln\left(\frac{a}{1-a}\cdot\frac{1-z}{z}\right)dz. \tag{C3}$$

REFERENCES

[1] K. Zhao, S. Lanzoni, Z. Gong, and G. Coco, "A numerical model of bank collapse and river meandering," Geophys. Res. Lett. **48**(12), e2021GL093516, https://doi.org/10.1029/2021GL093516 (2021).
[2] S. Ikeda, G. Parker, and K. Sawai, "Bend theory of river meanders. Part 1. Linear development," J. Fluid Mech. **112**, 363–377 (1981).
[3] G. Parker, K. Sawai, and S. Ikeda, "Bend theory of river meanders. Part 2. Nonlinear deformation of finite-amplitude bends," J. Fluid Mech. **115**, 303–314 (1982).
[4] P. Blondeaux and G. Seminara, "A unified bar–bend theory of river meanders," J. Fluid Mech. **157**, 449–470 (1985).
[5] P. Blondeaux and G. Seminara, "Corrigendum: A unified bar-bend theory of river meanders," J. Fluid Mech **193**, 599 (1988).
[6] N. Struiksma, K. W. Olesen, C. Flokstra, and H. J. De Vriend, "Bed deformation in curved alluvial channels," J. Hydraul. Res. **23**(1), 57–79 (1985).
[7] H. Johannesson and G. Parker, "Linear theory of river meanders," in *River Meandering*, edited by S. Ikeda and G. Parker, AGU Water Resource Monograph 12 (American Geophysical Union, 1989), pp. 181–214.
[8] G. Seminara and M. Tubino, "Weakly nonlinear theory of regular meanders," J. Fluid Mech. **244**, 257–288 (1992).
[9] G. Zolezzi and G. Seminara, "Downstream and upstream influence in river meandering. Part 1. General theory and application to overdeepening," J. Fluid Mech. **438**, 183–211 (2001).
[10] J. Imran, G. Parker, and C. Pirmez, "A nonlinear model of flow in meandering submarine and subaerial channels," J. Fluid Mech. **400**, 295–331 (1999).
[11] S. Z. Ali and S. Dey, "Hydrodynamics of a weakly curved channel," Phys. Fluids **31**(5), 055110 (2019).
[12] J. D. Smith and S. R. Mclean, "A model for flow in meandering streams," Water Resour. Res. **20**(9), 1301–1315, https://doi.org/10.1029/WR020i009p01301 (1984).
[13] G. Seminara, "Meanders," J. Fluid Mech. **554**, 271–297 (2006).
[14] G. Zolezzi, R. Luchi, and M. Tubino, "Modeling morphodynamic processes in meandering rivers with spatial width variations," Rev. Geophys. **50**(4), RG4005, https://doi.org/10.1029/2012RG000392 (2012).
[15] S. Dey and S. Z. Ali, "Fluvial instabilities," Phys. Fluids **32**(6), 061301 (2020).
[16] R. A. Callander, "Instability and river channels," J. Fluid Mech. **36**(3), 465–480 (1969).
[17] F. Engelund and O. Skovgaard, "On the origin of meandering and braiding in alluvial streams," J. Fluid Mech. **57**(2), 289–302 (1973).
[18] G. Parker, "On the cause and characteristic scales of meandering and braiding in rivers," J. Fluid Mech. **76**(3), 457–480 (1976).
[19] J. Fredsøe, "Meandering and braiding of rivers," J. Fluid Mech. **84**(4), 609–624 (1978).
[20] G. Seminara, G. Zolezzi, M. Tubino, and D. Zardi, "Downstream and upstream influence in river meandering. Part 2. Planimetric development," J. Fluid Mech. **438**, 213–230 (2001).
[21] M. Bolla Pittaluga, G. Nobile, and G. Seminara, "A nonlinear model for river meandering," Water Resour. Res. **45**(4), W04432, https://doi.org/10.1029/2008WR007298 (2009).
[22] S. Dey and S. Z. Ali, "Origin of the onset of meandering of a straight river," Proc. R. Soc. A **473**, 20170376 (2017).

[23]S. Z. Ali and S. Dey, "Hydrodynamic instability of meandering channels," Phys. Fluids **29**(12), 125107 (2017).
[24]R. Repetto, M. Tubino, and C. Paola, "Planimetric instability of channels with variable width," J. Fluid Mech. **457**, 79–109 (2002).
[25]R. Luchi, G. Zolezzi, and M. Tubino, "Bend theory of river meanders with spatial width variations," J. Fluid Mech. **681**, 311–339 (2011).
[26]A. Frascati and S. Lanzoni, "A mathematical model for meandering rivers with varying width," J. Geophys. Res. **118**(3), 1641–1657, https://doi.org/10.1002/jgrf.20084 (2013).
[27]E. C. Eke, M. J. Czapiga, E. Viparelli, Y. Shimizu, J. Imran, T. Sun, and G. Parker, "Coevolution of width and sinuosity in meandering rivers," J. Fluid Mech. **760**, 127–174 (2014).
[28]F. Monegaglia, M. Tubino, and G. Zolezzi, "Interaction between curvature-driven width oscillations and channel curvature in evolving meander bends," J. Fluid Mech. **876**, 985–1017 (2019).
[29]J. A. Constantine, T. Dunne, J. Ahmed, C. Legleiter, and E. D. Lazarus, "Sediment supply as a driver of river meandering and floodplain evolution in the amazon basin," Nat. Geosci. **7**(12), 899–903 (2014).
[30]C. F. Colebrook and C. M. White, "Experiments with fluid friction in roughened pipes," Proc. R. Soc. A **161**, 367–381 (1937).
[31]F. Engelund and E. Hansen, *A Monograph on Sediment Transport in Alluvial Streams* (Danish Technical Press, Copenhagen, 1967).
[32]S. Dey, *Fluvial Hydrodynamics: Hydrodynamic and Sediment Transport Phenomena* (Springer-Verlag, Berlin, Germany, 2014).
[33]S. Z. Ali and S. Dey, "Hydrodynamics of sediment threshold," Phys. Fluids **28**(7), 075103 (2016).
[34]S. Dey and S. Z. Ali, "Mechanics of sediment transport: Particle scale of entrainment to continuum scale of bedload flux," J. Eng. Mech. **143**(11), 04017127 (2017).
[35]S. Dey and S. Z. Ali, "Review article: Advances in modeling of bed particle entrainment sheared by turbulent flow," Phys. Fluids **30**(6), 061301 (2018).
[36]S. Dey and S. Z. Ali, "Bed sediment entrainment by streamflow: State of the science," Sedimentology **66**(5), 1449–1485 (2019).
[37]Z. Cao, G. Pender, and J. Meng, "Explicit formulation of the Shields diagram for incipient motion of sediment," J. Hydraul. Eng. **132**(10), 1097–1099 (2006).
[38]L. C. van Rijn, "Sediment transport, Part II: Suspended load transport," J. Hydraul. Eng. **110**(11), 1613–1641 (1984).
[39]A. M. Talmon, N. Struiksma, and M. C. L. M. Van Mierlo, "Laboratory measurements of the direction of sediment transport on transverse alluvial-bed slopes," J. Hydraul. Res. **33**(4), 495–517 (1995).
[40]E. Meyer-Peter and R. Müller, "Formulas for bed-load transport," in *Proceedings of the 2nd Meeting of International Association for Hydraulic Research*, Stockholm, Sweden (IAHR, 1948), Vol. 3, pp. 39–64.
[41]S. Z. Ali and S. Dey, "Origin of the scaling laws of sediment transport," Proc. R. Soc. A **473**, 20160785 (2017).
[42]M. Bolla Pittaluga and G. Seminara, "Depth-integrated modeling of suspended sediment transport," Water Resour. Res. **39**(5), 1137, https://doi.org/10.1029/2002WR001306 (2003).
[43]J. A. Jiménez and O. S. Madsen, "A simple formula to estimate settling velocity of natural sediments," J. Waterw., Port Coastal Ocean Eng. **129**(2), 70–78 (2003).
[44]B. Federici and G. Seminara, "Effect of suspended load on sandbar instability," Water Resour. Res. **42**(7), W07407, https://doi.org/10.1029/2005WR004399 (2006).
[45]M. B. Bertagni and C. Camporeale, "Finite amplitude of free alternate bars with suspended load," Water Resour. Res. **54**(12), 9759–9773, https://doi.org/10.1029/2018WR022819 (2018).
[46]R. K. Mahato, S. Z. Ali, and S. Dey, "Hydrodynamic instability of free river bars," Phys. Fluids **33**(4), 045105 (2021).
[47]S. Z. Ali, S. Dey, and R. K. Mahato, "Mega riverbed-patterns: Linear and weakly nonlinear perspectives," Proc. R. Soc. A **477**, 20210331 (2021).
[48]C. Camporeale, P. Perona, A. Porporato, and L. Ridolfi, "Hierarchy of models for meandering rivers and related morphodynamic processes," Rev. Geophys. **45**(1), RG1001, https://doi.org/10.1029/2005RG000185 (2007).
[49]P. K. Kitanidis and J. F. Kennedy, "Secondary current and river-meander formation," J. Fluid Mech. **144**, 217–229 (1984).